PNAS RESEARCH ARTICLE | APPLIED PHYSICAL SCIENCES

From relaxation to buckling: A continuum elastic framework connecting surface instabilities of highly compressed lipid thin films

Anna D. Gaffney[a,b,1], Dongxu Liu[b], Deepanjali Samal[b], Angelo R. Carotenuto[c], Luca Deseri[d], Massimiliano Fraldi[c,e], Ka Yee C. Lee[f], Luka Pocivavsek[b], and Nhung Nguyen[b,1]

Affiliations are included on p. 9.

Edited by David Weitz, Harvard University, Cambridge, MA; received February 4, 2025; accepted August 4, 2025

Self-assembled thin films respond to external loads via surface instabilities that are critical to their functionality in both biology and technology. Lipid monolayers at the air–liquid interface are one such system. Tunability between out-of-plane buckling (e.g., folding) and in-plane relaxation (e.g., reorganization of lipid domains) in highly compressed lipid monolayers suggests underlying mechanistic generality. Yet, how in-plane relaxation occurs and how it is distinguished from folding remains elusive. Here, we use continuum mechanics, finite element (FE) simulations, and Langmuir trough fluorescence microscopy (FM) data to elucidate the underlying mechanisms of these elastic instability modes. Uniaxial loading of the Langmuir trough is evaluated in FE simulations, where the lipid monolayer is modeled as a thin sheet with a hyperelastic energy function developed to exhibit a relaxation mechanism. Results show that this material relaxation mechanism triggers tunable in-plane shear localization (shear banding). Furthermore, the simulation results of a heterogeneous model, built from fluorescence micrographs of lipid domains distributed in a continuous matrix, are rigorously compared with experimental data by domain organizational analyses. These analyses suggest shear bands are sufficient in inducing domain symmetry breaking that is characteristic of in-plane relaxation and, without such shear bands, domain organization remains in powder structure, characteristic of folding lipid monolayers. Our findings develop a hyperelastic model validated against experimental FM images that can connect the observed lipid monolayer instabilities of folding and in-plane relaxation, establishing a generalized framework with the potential to unify all other monolayer instability modes and characterize other thin film systems.

lipid monolayer | finite element | thin films | elastic instability | shear banding

Significance

Using lipid monolayers as a representative system to study self-assembled thin solid films, this work integrates hyperelastic models with an in-plane relaxation mechanism driven by shear banding (localized shear deformations on a weaker global deformation field) to connect folding and in-plane relaxing surface instabilities in finite element simulations. The proposed general elastic framework can be extended to elastic systems including 2D or self-organizing materials, thin sheets, and active solids. Furthermore, as lipid interfaces are critical for various functions in living systems from cells to organisms, this work can be applied to other fields to increase our current understanding of living matter.

Thin films formed by the self-assembly of molecules at the air–liquid interface are prevalent in both biological and technological material systems. Their critical ability to regulate surface tension has been exploited in various structures including those associated with drug delivery (1–3), coatings in medical devices (4–7), electronic materials (8–11), and biological interfaces (12–16) to maintain interfacial structural stability in response to mechanical forces. Thus, Langmuir monolayers at air–liquid interfaces have been used extensively in biophysics, biochemistry, and nanotechnology as model systems to probe surface tension regulation and monolayer response to applied forces (17–20). A large body of work has been conducted on the liquid–liquid 2D phase transitions and morphologies of self-assembled thin sheets (17, 21–26). At low packing densities, the sheet exhibits a dominant fluid-like state with phase transitions governed by thermodynamic laws. At high levels of compression, a fluid-like sheet can evolve into a solid-like sheet, which has also been examined in previous studies (27, 28). From a mechanics point of view, the critical difference between a liquid and a solid sheet is the ability to support static shear stress (29, 30). While liquids can easily relax such stresses through viscous dissipation, solids cannot, giving rise to the various surface instabilities studied in thin solid films. It is well known that self-assembled thin sheets respond to high compressive forces with different modes of surface instabilities, the mechanical reversibility of which being an important factor in maintaining surface tension (31–42). Nevertheless, the underlying mechanism that dictates and unifies these modes in monolayers is far less understood.

Lipid monolayers are one experimental example of a thin sheet that undergoes phase transitions and instabilities in response to lateral compression (21, 32, 36). Biologically relevant in the eyes, ears, and lungs, the ability of these sheets to undergo reversible collapse

Author contributions: A.D.G., D.L., D.S., and N.N. performed research; A.D.G. analyzed data; A.D.G. and D.S. built and ran simulations; D.L. and N.N. wrote finite element implementation; A.D.G., D.L., K.Y.C.L., L.P., and N.N. wrote the paper; A.R.C., L.D., and M.F. provided theoretical insights and contributed analytic tools; and K.Y.C.L., L.P., and N.N. motivated and designed research.

The authors declare no competing interest.

This article is a PNAS Direct Submission.

[1]To whom correspondence may be addressed. Email: adgaffney@uchicago.edu or nhungng@uchicago.edu.

This article contains supporting information online at https://www.pnas.org/lookup/suppl/doi:10.1073/pnas.2502369122/-/DCSupplemental.

Published September 4, 2025.

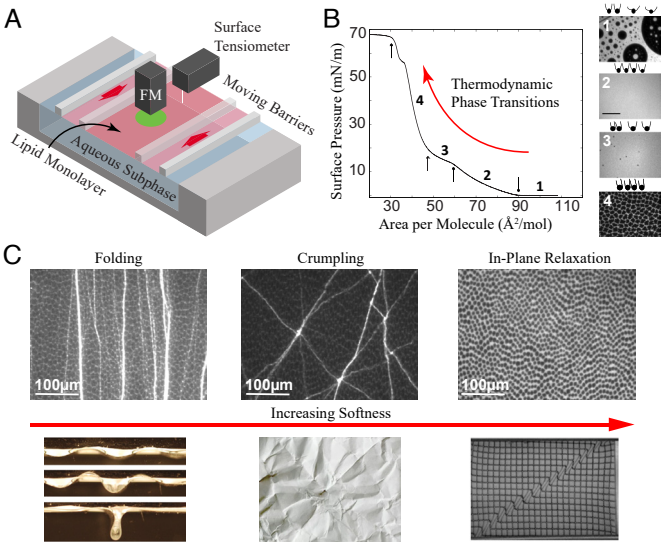

Fig. 1. Experimental method for probing lipid monolayer surface instabilities. (*A*) Schematic for the experimental setup of a Langmuir trough as utilized to capture all FM images within this text. (*B*) Surface pressure (difference between surface tension of lipid-free and lipid-covered interface) measured through surface tensiometer and different phases captured with FM during a Langmuir trough compression (41). (*C*) Three typical modes of surface instabilities in highly compressed lipid monolayers and corresponding instabilities well-known in solid mechanics: buckling of confined thin films (38), crumpling of thin sheets, and shear banding in granular materials (43).

and maintain mechanical stability is integral to their biological function and to the development of related medical treatments (12–16). Under unilateral compression in a Langmuir trough, both out-of-plane buckling and in-plane relaxation have been observed experimentally in highly compressed lipid monolayers (37). Yet, current mechanistic understanding of the correlation between these elastic instability modes is lacking. In this work, we model highly compressed lipid monolayers as elastic sheets where in-plane relaxation is controlled by the monolayer's ability to develop in-plane shear localization (shear banding). We validate our model against Langmuir trough experimental data where shear banding serves as a mechanism for differentiating out-of-plane folding and in-plane relaxation.

Experimental Instability in Lipid Monolayers. The mechanical properties of lipid monolayers are most often studied via unilateral compression in a Langmuir trough (Fig. 1*A*) with continuous fluorescence microscopy (FM) and surface tensiometry to probe the monolayer's multiscale response. Smaller scale techniques like atomic force microscopy (AFM) and X-ray diffraction can give molecular packing information (37, 44, 45), while larger scale techniques like surface viscosity measurements and Brewster angle microscopy can provide additional insight toward bulk material properties and surface deformations (45, 46). While a broad range of material behaviors are exhibited by lipid monolayers, a large portion of experimental systems sequentially undergo two forms of surface responses over the course of compression: first, molecular phase transitions from gas, to liquid-like ("expanded"), to solid-like ("condensed") (23, 47, 48), and second, surface instabilities (36). During the liquid-like phase of many observed cases (27, 45, 49–51), the monolayer becomes highly heterogeneous with condensed lipid domains (dark) dispersed in a soft matrix (light) (Fig. 1*B*). In solid-like lipid monolayers, reversible out-of-plane instabilities (Fig. 1*C*) such as crumpling (out-of-plane buckling with point and line singularities) and folding (localized but smooth out-of-plane buckling that is dominated by bending and stretching) have been extensively studied (41, 52–55). Recently, a new mode of instability where the lipid monolayer relaxes in-plane leading to a banded morphology of condensed domains was discovered (Fig. 1*C*) (37, 41). Interestingly, all of these solid instabilities resemble well-known problems in traditional solid mechanics, including buckling of confined thin films (38, 52, 56), crumpling of thin sheets (57, 58), and shear banding in granular materials (Fig. 1*C*) (43, 59, 60).

Experiments have shown that tuning the softness of the lipid monolayers by modifying lipid composition or temperature can tune collapse phenomena from out-of-plane folding/crumpling to in-plane relaxation (41, 49, 61, 62). Fig. 2 focuses on one such compositional example, contrasting the in-plane domain morphologies of two monolayers (one that folds vs. one that relaxes in-plane) at two points: 1) start of the elastic regime, low lateral pressure and 2) high lateral pressure, as published in Pocivavsek, et al. (37). The defining characteristic of in-plane relaxation in lipid monolayers is the reorganization of condensed domains from roughly hexagonal (powder) structure to a banded morphology, where the spatial symmetry is broken and domains become closer in one direction and farther in the opposite direction. This feature is not observed in lipid monolayers that fold, where the powder structure persists until the point of

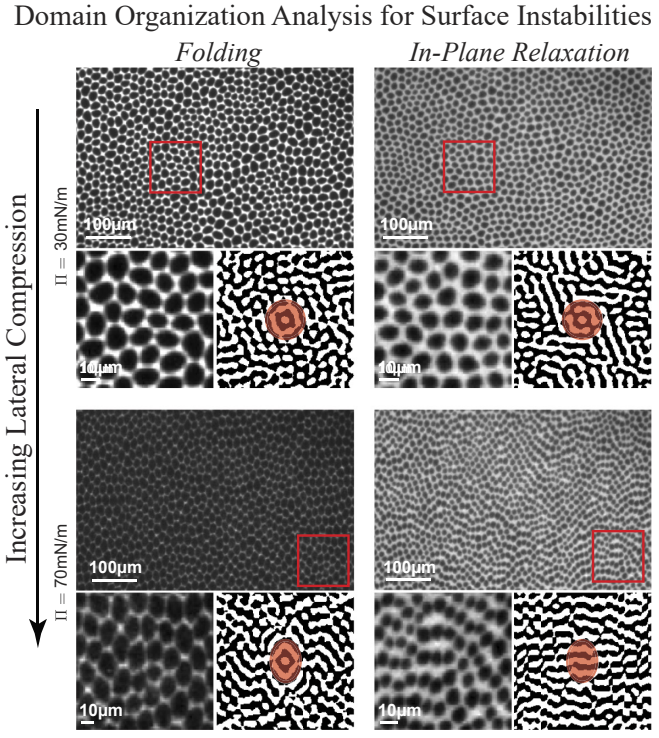

Fig. 2. Evolution of condensed domain (dark ovals) organization captured by FM for monolayers that lose stability via folding (*Left*) and relaxing in-plane (*Right*) (compositional details found in *Materials and Methods*) under increasing lateral compression, as previously published (37). A representative local packing morphology is shown below each image, with its 2D image autocorrelation to the *Right*. The autocorrelations show that for folding lipid monolayers, the condensed domains maintain powder structure with increasing lateral compression prior to out-of-plane instability (the filled red areas in the autocorrelations of the *Left* column show similar circle and ring). For in-plane relaxing monolayers, the powder structure that exists at low compression is disturbed at high compression, where distinct bands of condensed domains are emphasized in the autocorrelation (the filled red areas in the autocorrelations of the *Right* column show a circle and ring at low compression, while distinct lines are shown at high compression).

folding out-of-plane. To quantify this feature globally, our past work conducted Fourier transforms of 2D autocorrelations of FM images (37). In the current work, we focus on more local morphologies in order to later compare with computational results. We quantitatively characterize this feature using 2D autocorrelations, as described in *Materials and Methods*, with the analysis of representative local organizational morphologies shown in Fig. 2 and *SI Appendix*, Fig. S2*A*.

Folding in various self-assembled monolayer systems including lipids and gold nanoparticles has successfully been modeled using elastic plate theory, where out-of-plane buckling is driven through an energy balance of in-plane compression and out-of-plane bending (35, 37, 38). As noted above, folding has been linked to a preserved in-plane domain packing structure throughout the elastic regime. The ability of domains to break the symmetry of their hexagonal packing and reorganize in-plane into bands suggests the need to explore another mechanism that the lipid monolayer may undergo within the elastic regime to relax in-plane loading. These aspects remain poorly understood and no current work has shed significant insights into the differences in experimental observations as presented in Fig. 2.

Modeling Instability in Lipid Monolayers. Many theoretical and computational approaches have been developed at the molecular level to study the instability of lipid monolayers. Incorporating thermodynamics principles, where equations of state and defects were used to describe the phase transition in lipid monolayers (18, 21, 23), folding onset was captured by minimizing the interfacial energy. Molecular dynamics simulations showed the appearance of undulations followed by the transition to a single fold into the aqueous subphase upon increasing lateral compression (39, 63, 64). Yet, the simulated undulation and fold are on the order of lipid monolayer thickness due to the limited size (nanometer) of these simulations. Thus, while providing valuable insights into molecular interactions that underlie the onset of out-of-plane instabilities, these approaches have not successfully explained the three order of magnitude difference in the fold length scale (micron) as compared to thickness (nanometer). Alternatively, studies that utilize a continuum mechanics approach were proposed to quantitatively characterize folding of both lipid and gold nanoparticle films (38, 52, 56, 65, 66). Here, the Langmuir monolayer is considered as a uniform elastic plate that buckles under lateral compression. A simple model was developed by Ries for solid-like response of highly compressed monolayers where the hypothesis of elastic plate buckling is used to explain the appearance of a tall fold atop the monolayer (52). The wrinkle-to-fold model further extends this assumption to study the peculiar folding behavior in monolayers of lipid and gold nanoparticles (38). It shows that the films go through wrinkling with micron-size wavelength determined by the relative stiffness of the monolayer and the liquid subphase. Under further compression, these wrinkles localize into large folds observed experimentally. Thus, this reduced geometric approach can provide a highly quantitative mechanistic understanding of experimental observations.

Relatively fewer efforts have focused on modeling in-plane relaxation in lipid monolayers. Some studies suggest the similarity with flow-induced shear bands in complex fluids and granular materials (67–69). Other recent attempts aim to enrich material models by extending the success of modeling folding lipid monolayers as homogeneous elastic plates to in-plane relaxation. As monolayer folding can be described with neo-Hookean and other hyperelastic models, efforts are devoted to extending the conventional hyperelastic models to capture in-plane relaxation (38, 52). Specifically, models that invoke irreversibility either through inelastic material behavior (e.g., viscoplasticity) or nonlinear elasticity with two-slope stiffnesses (e.g., bielastic) were discussed (41). In our recent work, we instead assumed that the lipid monolayer mechanically behaves like a hyperelastic material, storing elastic energy both through local volume and shape changes of the continuum (70). The onset of shear band bifurcations was characterized through an incremental approach to nonlinear elasticity and, informed by experimental isotherms of lipid monolayers, we found that hyperfoam-like energetics were able to replicate the observed hardening during the elastic regime before a point of instability and obtain theoretical predictions of the critical pressures. This work indicated that material instability on the nonlinear elastic response of the continuum representing the lipid monolayer, through shear banding, could be a potential feature associated with in-plane relaxation. Nevertheless, a finer-scale in silico investigation capable of reproducing the experimental post-critical domain reorganization (Fig. 2) remains an unresolved challenge.

The tunable nature of experimental lipid monolayer instabilities further necessitates the development of a new computational model with an appropriate constitutive equation that can capture the distinct experimental observation of domain morphology in both folding and in-plane relaxing lipid monolayers. In this work, we show that in-plane domain organizational symmetry breaking can be achieved by allowing the matrix to release compressive load via regions of highly localized shear strain, or shear bands. We first establish a constitutive model that can tune shear band onset and strength. The ability to trigger or not trigger shear banding in the material model is assumed to be associated with the ability of the lipid monolayer to undergo in-plane or out-of-plane instability, respectively. We further explore these instability modes through modeling thin sheet instabilities in response to lateral compression via finite element (FE) analysis. We start with a homogeneous representation of lipid monolayers and then enrich the computational model with the heterogeneous domain organization captured in FM imaging, performing a rigorous comparison between FE modeling and experimental data. We develop a hyperelastic model validated against experimental FM images that can connect the observed lipid monolayer instabilities of folding and in-plane relaxation, establishing a generalized framework with the potential to unify all other monolayer instability modes and characterize other thin film systems.

Results and Discussion

Tunable Material Model for In-Plane Relaxation in Lipid Monolayers. Building upon the success of linear elasticity to describe folding (38, 52), we are motivated to maintain a purely elastic approach to capture other modes of instability in lipid monolayers. Recently, hyperelastic models have had some preliminary success in the endeavor to describe in-plane relaxation (70). We develop a more general and tunable hyperelastic energy functional to model highly compressed lipid monolayers as thin, elastic sheets with the ability to release in-plane compressive load through shear localization (shear banding) triggering monolayer in-plane relaxation. The model can independently toggle three regimes of the material response: first elastic regime, relaxation regime, and second elastic regime (*SI Appendix*, Fig. S1 and Fig. 3), which can efficiently produce a broad range of shear banding behavior, where the degree of nonmonotonicity in the shear stress–strain

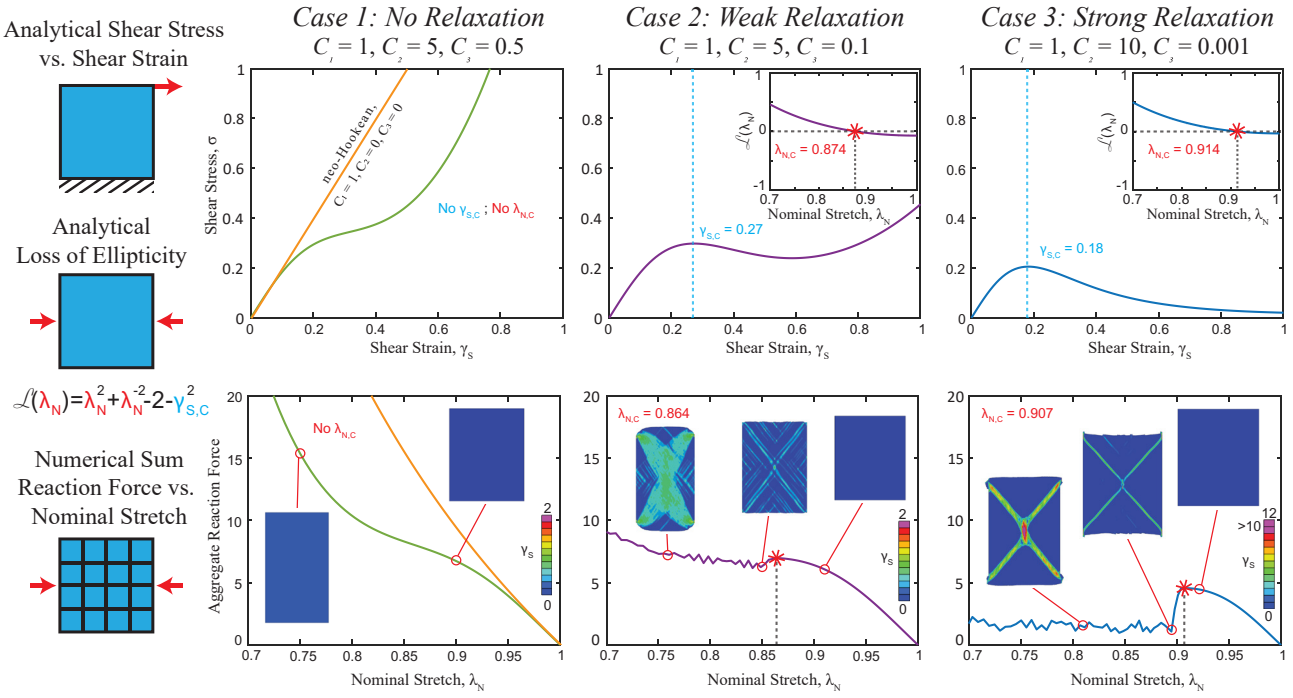

Fig. 3. Tuning 3 cases of shear band onset and behavior in a homogeneous model. *Top* Row: Plots present shear stress–strain responses under simple shear loading (schematic *Top Left*; see *SI Appendix*, Eq. **S7**). The *Inset* figures depict analytical loss of ellipticity for a unilateral compressive loading (schematic *Middle Left*; see *SI Appendix*, Eq. **S6**), which leads to the determination of the critical value ($\lambda_{N,C}$) of the nominal stretch λ_N, at which shear bands occur. Analytical predictions indicate no relaxation onset for Case 1, due to its monotonic shear stress–strain response, and onsets of relaxation for the last two cases, which show nonmonotonic shear stress–strain responses. The neo-Hookean material used successfully to study folding is also presented in the plot of Case 1, showcasing model tunability. *Bottom* Row: Plots show the material responses for FE simulations of the unilateral compression of a homogenous model (schematic *Bottom Left*) where the material is described by the corresponding shear stress–strain response in the *Top* row. Shear banding onset ($\lambda_{N,C}$) is associated with the peak in reaction force, which is in good agreement with the analytical prediction for all three cases (corresponding star symbols in *Top* row *Inset* vs. *Bottom* row). *Inset* in each plot are representative field distributions of shear strain in FE simulations over the course of compression. A homogeneous deformation field is maintained in Case 1. In Case 2, shear bands form and become more dilute in the second elastic regime. Last, in Case 3, sharp shear bands occur and persist over the entire numerical simulation.

response is found to significantly impact the strength and persistence of shear banding. We test the tunability of this model using FE simulations in a uniaxial loading configuration to emulate the Langmuir trough, then applying this model to a more complex 2D hard-soft composite with domain organizational morphology derived from an experimental lipid monolayer FM image.

Nonmonotonic hyperelastic material model allows for in-plane relaxation via the formation of shear bands: Homogeneous representation of lipid monolayers. In continuum mechanics, a 2D shear band can be characterized mathematically as an area, surrounded by shocklines, where the shear strain is significantly higher than outside, leading to the majority of the shear deformation localizing within the shear band (60). This redistribution of strain allows for in-plane relaxation. While multiple modeling approaches have been developed to describe shear banding, there has been very limited theoretical work put toward applying shear banding to lipid monolayers (70). Importantly, no model has yet captured the symmetry breaking of condensed domain organization, which is the experimental hallmark of in-plane relaxation in lipid monolayers. In this work, with the goal to propose a simple and tunable constitutive model, we adapt an existing constitutive equation developed by Seki and Alturi (71). We develop an understanding for its computational applications in lipid monolayers, emphasizing its ability to form shear bands as the feature that we propose governs the mechanism for in-plane relaxation. The response from this model described by an incompressible hyperelastic-type energy function (see details in *Materials and Methods*) is dictated by 3 material properties: (C_1, C_2, C_3) where C_1 controls the first elastic regime, C_2 controls the relaxation regime, and C_3 controls the second elastic regime, further discussed in *SI Appendix*, section 2 and shown in *SI Appendix*, Fig. S1. The influence of the corresponding response in simple shear on shear banding onset in a uniaxial compression is also examined by the standard loss of ellipticity analysis in continuum mechanics (60, 72) (through the "equilibrium shock" approach (73); see *Materials and Methods* and *SI Appendix*, section 3). With a focus on shear banding tunability of this model as an underlying mechanism for tunability between folding and in-plane relaxation, we highlight here three typical cases: (Case 1: $C_1 = 1, C_2 = 5, C_3 = 0.5$; Case 2: $C_1 = 1, C_2 = 5, C_3 = 0.1$; Case 3: $C_1 = 1, C_2 = 10, C_3 = 0.001$) and analyze shear banding of the corresponding constitutive model (Fig. 3). The first case shows a monotonic shear stress–strain response in simple shear indicating no relaxation (Fig. 3, *Top* row). Note that the typical neo-Hookean case used to describe folding lipid monolayers is also obtained from this model with appropriate specifications of the 3 material parameters ($C_1 = 1, C_2 = 0, C_3 = 0$). The last two cases exhibit nonmonotonic responses: Case 2 exhibiting a short-term drop in shear stress σ when the shear strain $\gamma_S = \gamma_{S,C}$ and Case 3 exhibiting a long-term drop in σ when $\gamma_S = \gamma_{S,C}$. For the nonmonotonic cases, loss of ellipticity analyses indicate the onset of the desired shear banding phenomena, where the point of shear stress relaxation in simple shear can be considered as the critical point of shear band onset $\gamma_{S,C}$ (see Fig. 3, *Top* row *Insets*, and *Materials and Methods*).

Given the unique loading conducted on lipid monolayers with a Langmuir trough, we first simulate in-plane uniaxial compressive loading on a homogenous FE model as described

in *Materials and Methods*. We characterize the effective behavior of the material through recording the reaction force along one vertical boundary as a function of the nominal stretch, $\lambda_N = L/L_0$, where L and L_0 are the deformed and undeformed width of the FE model, respectively. The point where the reaction force drops is the critical nominal stretch $\lambda_{N,C}$. As described in *SI Appendix*, section 3 and shown in Fig. 3, this computational critical point (signified by stars in the *Bottom* row of Fig. 3) is within 1% error of the analytical onset of relaxation as determined from the loss of ellipticity analysis (signified by stars in *Insets* in the *Top* row of Fig. 3), validating that the computational model is accurately exhibiting the chosen material response. For the parameter sets that do not analytically provide a relaxation point, such as Case 1 and neo-Hookean, the computational result shows no drop in reaction force. The consistent agreement between analytical and FE model in determining shear banding onset emphasizes the proposed constitutive equation as well-controlled in its ability to differentiate between relaxation and no relaxation for a system with the geometry and load state similar to lipid monolayers.

The representative field distributions of shear strain in the FE simulations (Fig. 3, *Bottom* row *Inset*) show how the proposed constitutive equation can tune both shear banding onset and behavior. Specifically, for cases where the shear stress–strain relationship in simple shear is monotonic and exhibits no relaxation point, there is no instability in the material's shear deformations (e.g., Case 1 and neo-Hookean). In cases where the shear stress–strain relationship in simple shear is nonmonotonic, distinct shear bands form in the material when $\lambda_N = \lambda_{N,C}$ (e.g., Cases 2 and 3). Furthermore, the degree of nonmonotonicity in the shear stress–strain response is found to significantly impact the strength and persistence of shear banding. Low nonmonotonicity is exhibited by Case 2, where the relaxation regime of the shear stress–strain relationship in simple shear has a small slope, causing weak shear bands to form, and returns to the second elastic regime with little added strain, causing the dissolution of shear localization. High nonmonotonicity is exhibited by Case 3, where the relaxation regime has a larger change in slope and the second elastic regime is not reached within the computational model's loading, creating strong and persistent shear bands over the course of compression. The difference between shear strain within the band to outside the band for Case 3 is 5 times as large as that of Case 2, further showcasing the difference in behavior of these two parameter sets.

We have identified and tested a constitutive equation that, when applied to a flat plate under uniaxial lateral compression, exhibits tunable shear banding onset and behavior in FE simulations. In the next section, this constitutive equation will be applied to the continuous matrix of a heterogeneous FE model to connect these results to the realistic biphasic representation of lipid monolayers. We will show that this shear banding material response can trigger in-plane relaxation in lipid monolayers, specifically with shear bands in the soft continuous matrix leading to symmetry breaking of the condensed domain morphology as seen by FM.

Nonmonotonic hyperelastic matrix driving shear bands allow for in-plane relaxation via domain reorganization: Heterogeneous lipid monolayers. The FE model using a homogeneous representation of lipid monolayers is extended to incorporate the presence of condensed domains surrounded by a softer matrix. Specifically, we constructed a FE model starting with the lipid monolayer domain organization obtained via a FM image of a lipid monolayer at the start of the elastic regime with powder domain structure (37) (see Fig. 2 and *Materials and Methods*).

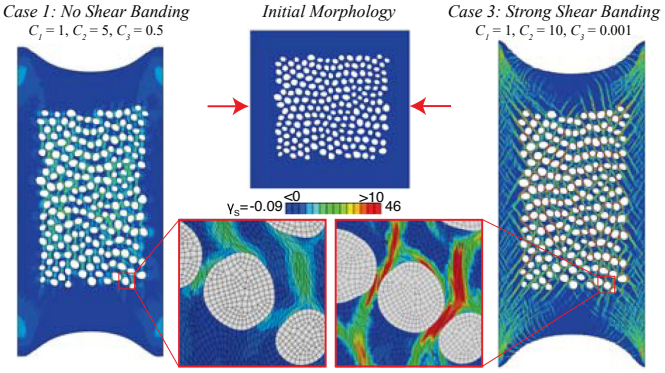

Fig. 4. Representative field distributions of shear strain for FE model built from FM images of a lipid monolayer at the start of the elastic regime with powder domain structure (Fig. 2). Significantly less localized shear strains are seen in FE model implementing a monotonic shear stress–strain response (Case 1 in Fig. 3, *Left*), while strong shear bands, occurring as shocklines, form in the matrix for the nonmonotonic shear stress–strain response, promoting condensed domain reorganization (Case 3 in Fig. 3, *Right*).

We then simulated the unilateral loading similar to the homogeneous case to mimic the compressive process in Langmuir trough experiments. Our prior work (37) has indicated that key structural differences between lipid monolayers that fold and relax in-plane exist within the continuous matrix. As such, we take the approach of modeling the continuous matrix with the 3 cases of tunable shear banding material as developed above, while the condensed domains are modeled as simple neo-Hookean elastic inclusions (*Materials and Methods*). For Case 1, where the system does not exhibit shear bands in the homogeneous system, no shear bands form in the matrix (Fig. 4, *Left*). For Case 3, shear bands form between the domains on diagonals in the form of strong localized regions of shear strain that allow for domains to break their hexagonal symmetry, coming closer in the lateral direction than the vertical (Fig. 4, *Right*). Note, the material within the shear bands of Case 3 is being deformed on the order of 10× as much as the most strained material between domains in Case 1, as seen in the maximum strain values of Fig. 4. Case 2 also exhibits the emergence of shear bands, which dissolve over the course of the simulation similar to what is seen in the homogeneous case, with the final strain localization very similar to that of Case 1 (Movie S2). The consistency of shear banding onset and behavior between the homogeneous and heterogeneous FE models suggests a robust nature of the proposed constitutive equation.

Much of the current theory behind instabilities in lipid monolayers implicate condensed domain phase boundaries in the triggering of folds (32, 54). It should be noted that our results show that the addition of condensed domains is not sufficient to impose shear bands in a material that does not form shear bands in a homogeneous model (see Case 1 in Fig. 4 and *SI Appendix*, Fig. S2*C*). On the other hand, simulations suggest that the capability of the matrix to relax in-plane load, which can be tuned through our proposed constitutive model, plays the critical role in triggering instabilities and breaking symmetry of domain organization. Varying shape and size of the domains also does not affect the formation of shear bands in the matrix, as seen in validation against two additional previously published experimental compositions (37) (*SI Appendix*, Fig. S2*C*). These simulations provide insightful information of how domains impact the formation and organization of shear bands and the mechanisms that dictate different modes of elastic instability. They also enrich the current continuum model that is only applicable to folding lipid monolayers. Last, the localization of shear bands in Case 3 throughout compression

supports our hypothesis that shear bands between domains may be an important underlying mechanism to in-plane relaxation in lipid monolayers and leads us to assess their effect on domain organizational morphology.

Model Validation with Experimental Data: Analysis of Domain Organizational Morphology. In the Langmuir trough experiment, in-plane relaxation is evaluated by domain organizational morphology via FM. To further confirm that our FE model can capture and tune between lipid monolayers that exhibit different instability modes, in this section, we provide a comparison to experimental results.

Finite element model captures in-plane relaxation signature from experimental images. As presented in the Introduction, in-plane relaxation in Langmuir trough experiments is characterized by the reorganization of domains from powder structure to lines of condensed domains with broken organizational symmetry. This pattern is emphasized via image analysis, utilizing 2D autocorrelation (Fig. 2). Specifically, as presented in *Materials and Methods*, the powder structure domain organization in the 2D autocorrelation can be characterized as a circle and ring for nearest neighbors with disordered long range spatial correlation, as seen in the experimental monolayer that folds (Fig. 5 *Top*, *Left*). The in-plane relaxation organization can be characterized in the 2D autocorrelation as persistent stripes from short to long range, seen in the experimental example (Fig. 5 *Top*, *Right*). The same approach is applied to analyze the domain organizational morphology from FE models of two heterogeneous lipid monolayers in which the matrix is modeled with Case 1 (no shear bands) (Fig. 5 *Bottom*, *Left*) and Case 3 (strong shear bands) (Fig. 5 *Bottom*, *Right*). Results for the domain morphology in Fig. 5 show that the resultant autocorrelation for Case 1 (no shear bands) has the characteristic circle and ring, recreating the local experimental in-plane organization of a folding monolayer. In direct comparison, the resultant autocorrelation for Case 3 (strong shear bands) has the characteristic persistent stripes from short to long range, recreating the experimental broken-symmetry organization of in-plane relaxation (Fig. 5). We further validate that shear bands induce organizational symmetry breaking by assessing the resultant signatures of two additional experimental compositions (37) (*SI Appendix*, Fig. S2 *A* and *B*). Experimentally, these two systems undergo folding and in-plane relaxation, respectively. In the FE simulation, these models can reproduce the resultant domain organization of their experimental counterparts or be

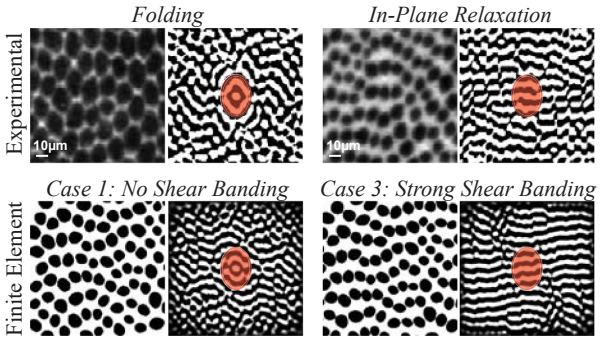

Fig. 5. Validation against experimental data (37) as shown in Fig. 2. *Left* Column: Simulations without shear band formation in the matrix (Case 1) show maintained powder structure at high compression, highlighted with 2D image autocorrelations, much like that of experimental folding lipid monolayers. *Right* Column: Simulations with strong shear band formation in the matrix (Case 3) show similar domain organization to that observed in in-plane relaxing lipid monolayers, also highlighted using 2D image autocorrelations.

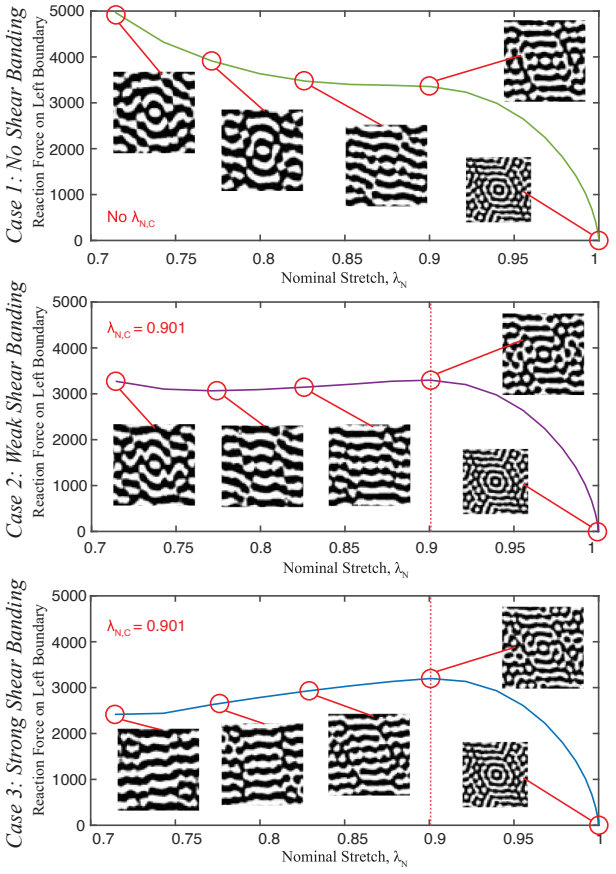

Fig. 6. Progression of condensed domain organization obtained from heterogeneous FE models, analyzed with 2D image correlation. Three cases for the material model (Fig. 3) are applied to the continuous matrix. For each case, the reaction force of the left boundary is plotted against the nominal stretch, with *Insets* showcasing transient organization analyzed with 2D autocorrelations.

tuned to capture the opposite response via controlling shear band formation in the matrix. This suggests that strong shear banding in the matrix is sufficient to break the symmetry of a powder structure domain organization as seen experimentally. Our FE models can capture and tune between the distinct characteristic domain organizations for both lipid monolayers that fold and those that relax in-plane.

Tuning progression of domain organization throughout compression. While Fig. 5 showcases the endpoint of the simulations, we can also gain valuable insights by assessing the reaction force and transient domain organization over the course of compression. Overall, the reaction force response of the heterogeneous simulations mimics the response of those without domains as seen in Fig. 3: Case 1 exhibits a monotonic shear stress–strain relationship, Case 2 exhibits a nonmonotonic relationship with a weaker and shorter relaxation, and Case 3 exhibits a strong and persistent relaxation (Fig. 6). What is especially interesting, however, is the progression of the autocorrelation signature for each of these cases. Case 1 exhibits a slight loss of symmetry at its inflection point, while returning to a stretched powder structure as the compression develops further and reaction force continues to increase. Case 3 provides a clear example of a 2D autocorrelation morphing from powder structure to the signature of in-plane relaxation. The circle and ring signature steadily loses its symmetry as it converts into persistent lines. The most dynamic transient morphing is shown in Case 2. With a matrix

material that forms shear band strain localizations which then quickly dissolve, Case 2 exhibits a stronger loss of symmetry than that of Case 1 immediately after the onset of shear bands, closely resembling the autocorrelation signature of Case 3 (strong shear banding). However, toward the end of the simulation, as the shear bands dissolve, the autocorrelations quickly revert to a stretched powder structure, with the endpoint autocorrelation signature similar to that of Case 1 (no shear banding).

In summary, through exploring a hyperelastic model for lipid monolayers integrated with validated FE simulations, we are able to impose and modulate shear bands in both homogeneous thin sheets and thin sheets with stiff inclusions mimicking condensed domains. With an experimental lipid monolayer FM-derived domain organization as the initial structure, we are able to compare resultant deformed organizational structures directly to those of the experimental systems. From the quantification of these packing structures in the form of 2D autocorrelations, we find that the formation and persistence of shear bands in the matrix between domains are sufficient in reproducing the in-plane relaxation signature from experiments. And with the dissipation of such shear bands, that reproduction is lost and domain packing returns to a powder structure. The unique strength of a hyperelastic material with a nonmonotonic shear stress–strain relationship is its ability to impose a temporary relaxation. This model in particular is also built with strong tunability, showcased by its ability to capture not only hexagonal packing (no shear banding in Case 1) and in-plane relaxation (strong shear banding in Case 3) but also the morphing of domain packing structures (weak, transient shear banding in Case 2). This mimics the experimental system, as lipid monolayers can exhibit other modes of instability between folding and in-plane relaxation.

Conclusions

Highly compressed lipid monolayers exhibit a range of surface instability modes, with experimental tunability that suggests underlying mechanistic generality. Prior to this work, folding lipid monolayers have successfully been characterized as continuum elastic thin sheets (38, 52, 56). However, it remains unclear whether this elastic framework can extend to other surface instabilities, and if so, which elastic material model can successfully capture all observed instability modes. In this work, we develop a hyperelastic model validated against experimental FM images that can connect the observed lipid monolayer instabilities of folding and in-plane relaxation, establishing a generalized framework with the potential to unify all other monolayer instability modes. This model integrates a relaxation mechanism in the shear stress–strain response obtained from a hyperelastic energy function to trigger and tune shear banding behavior, as verified with homogeneous FE simulations that simulate the experimental lateral compression. To capture the main characteristic that distinguishes between folding and in-plane relaxation modes in lipid monolayers (condensed domain organization), we implement this model in the softer continuous matrix of a heterogeneous FE simulation, with initial stiff domain organization derived from experimental FM data. We conclude that shear bands are sufficient in inducing domain symmetry breaking that is characteristic of in-plane relaxation, and without such shear bands, domain organization remains in powder structure, as seen in folding lipid monolayers. Furthermore, by assessing the autocorrelation signatures throughout the compression process for matrices with different shear banding behavior, transient modes of surface instabilities between folding and in-plane relaxation are captured. This general elastic framework has the potential to extend to other elastic systems which meet the criteria of being 2D thin films under thermodynamic equilibrium with material conservation. This subset of systems includes, but is not limited to, lipid monolayers of various compositions (45, 61, 74) and block-copolymer monolayers, which have been shown to exhibit in-plane relaxation and reorganization of stiff cores similarly to lipid monolayers (24–26, 42). There is also the potential to build connections between model parameters and more physical scenarios by incorporating comparative bulk material properties [e.g., surface viscosity and bulk moduli (45)] for experimental systems under the defined criteria. AFM, specifically, has been utilized to capture nanodomains within lipid monolayers (37, 41), with the ability to determine comparative compliance or "softness" between nanodomains and the matrix (45). This information can provide further insight for a more physical material model. While some materials, such as Gibbs monolayers of soluble lipids (75), do not meet the criteria needed to be modeled by this framework, future work can add complexity to explore dynamic material exchange, rate dependence, and out-of-plane surface instabilities. Overall, this work provides effective behavior that can be utilized in probing the smaller-scale underlying mechanisms [e.g., based on Structured Deformations (76–79)] and is generally applicable to surface instabilities in many other thin sheet systems.

Materials and Methods

Experimental Lipid Monolayer Compression Measurements. Experimental data used for comparison and validation to our developed computational model utilize FM micrographs of four lipid monolayer compositions deposited and compressed on a Langmuir trough, as published previously by Pocivavsek et al. (37). The two compositions shown in Figs. 2 and 5 are 7:3 dipalmitoylphosphatidylcholine (DPPC):palmitoyloleoylphosphatidylglycerol (POPG) (folding) and 7:3 DPPC:POPG with 10 wt% lung surfactant protein SP-B_{9-25} (in-plane relaxation) at 25 °C. The two compositions shown in *SI Appendix*, Fig. S2 are 8:2 DPPC:ganglioside G_{M1} (folding) and 5:5 DPPC:G_{M1} (in-plane relaxation) at 30 °C. As described in the published methods, the solutions were diluted to obtain spreading solutions of concentration 0.1 mg ml^{-1}. The fluorescent probe used for visualization at 0.5 mol% with FM was Texas Red 1,2-dihexadecanoyl-sn-glycerol-3-phosphoethanolamine (TR-DHPE) (Molecular Probes, Eugene, OR). Fluorescently labeled lipids at this minimal concentration have been shown not to significantly affect phase behavior or surface instability, as shown via comparison to label-free isotherms (80) and other methods such as polarized fluorescence and Brewster angle microscopy (46). When the monolayer is highly compressed and the domains take up a large surface area fraction, the concentration of dye in the matrix increases, which could have an effect on microstructure within the matrix. Research utilizing water-soluble fluorescent dyes for lipid monolayers (which provides visualization of domains while maintaining constant dye concentration in the matrix via desorption) found that, while improving contrast, this technique did not affect phase behavior of the studied compositions, which include lipids DPPC and POPG (74). Extension into other compositions may require further exploration into the influence of fluorescently labeled lipids. These samples were deposited on ultrapure water under ultrahigh purity argon to minimize oxidative damage. The instrument used to collect these data was a custom-made Teflon trough equipped with two Teflon barriers whose motions were precisely controlled for symmetric uniaxial lateral compression with a linear speed of 0.1 mm s^{-1} (Fig. 1*A*). A stationary Wilhelmy balance (Riegler and Kirstein, Berlin, Germany) was used to measure surface pressure.

Image Analysis. We can describe the spatial distribution of regions showing high (bright matrix) and low (dark condensed domains) levels of fluorescence using an adaptation of previously published methods (37). This work showcases local domain organization, since our FE models utilize a portion of the FM micrograph morphology. We first filter to remove high and low frequency noise

associated with nonuniform illumination. Then, we conduct a 2D autocorrelation of a portion of the domain organization, designated for experimental FM images with a red square. These autocorrelations indicate the rate of decay in positional correlation between bright and dark regions in the image. This means the signature at the center of the autocorrelation refers to average nearest neighbor spacing, while the structures formed away from the center refer to spacing farther away. In most autocorrelation figures in this work, we bring focus to the nearest neighbor morphology by adding a red semitransparent circle or oval.

Material Model. In this work, a hyperelastic model is proposed by developing the model of Seki and Atluri (71) to describe and model the behavior of a lipid monolayer matrix, given as

$$\psi = \widehat{\psi}\left(\mathbf{C}\right) = \frac{C_1\left(\bar{I}_1 - 3\right)}{\left[1 + C_2\left(\bar{I}_1 - 3\right)\right]} + C_3\left(\bar{I}_1 - 3\right)^2 + \frac{K}{2}\left(J-1\right)^2, \quad [1]$$

where $\bar{I}_1 := tr\bar{\mathbf{C}} = J^{-2/3}tr\mathbf{C}$ is defined as the first invariant of $\bar{\mathbf{C}}$, with $tr(\bullet)$ the trace of a tensor, K is the bulk modulus, C_1, C_2, and C_3 are material parameters. Note that $C_1 = \mu/2$, where μ is shear modulus.

From this strain energy function, the constitutive model can be derived (see details in *SI Appendix*, section 1):

$$\sigma = \left\{\frac{2C_1}{1 + C_2\left(\bar{I}_1 - 3\right)} - \frac{2C_1C_2\left(\bar{I}_1 - 3\right)}{\left[1 + C_2\left(\bar{I}_1 - 3\right)\right]^2} + 4C_3\left(\bar{I}_1 - 3\right)\right\} \cdot J^{-5/3}\left(\mathbf{B} - \frac{I_1}{3}\mathbf{I}\right) + K(J-1)\mathbf{I}. \quad [2]$$

Loss of Ellipticity Analysis for Shear Banding. A 2D shear band can be characterized mathematically as an area, surrounded by shocklines, where the shear strain is significantly higher than outside. As described in Seki and Atluri (69), there exists for some $\gamma_1 \neq \gamma_2$ the following inequality given by Abeyaratne and Knowles (71) where shocklines exist in plane strain incompressible materials.

$$[\tau(\gamma_1) - \tau(\gamma_2)][\gamma_1 - \gamma_2] \leq 0. \quad [3]$$

The equivalence between this condition and the singularity of the acoustic tensor for the associated incremental problem, pursued in (68), can be found in (70). Equation 3 means that loss of ellipticity occurs when the slope of the shear stress–strain relationship transitions from positive to negative, at some critical shear strain, $\gamma_{S,C}$. The loss of ellipticity condition is used to determine the critical point where a uniaxial compression experiences shear deformation by assessing the following equation for the equivalent amount of shear strain in a two-dimensional case

$$\gamma_S{}^2 = tr(\mathbf{B}) - 2, \quad [4]$$

where $\mathbf{B}$ is the left Cauchy–Green deformation tensor for a uniaxial compression of a quasi-incompressible material in terms of nominal stretch, $\lambda_N = L/L_0$, given by the following equation

$$\bar{\mathbf{B}} := \bar{\mathbf{F}}\bar{\mathbf{F}}^T = \begin{bmatrix}\gamma_N & 0\\ 0 & \gamma_N{}^{-1}\end{bmatrix}\begin{bmatrix}\gamma_N & 0\\ 0 & \gamma_N{}^{-1}\end{bmatrix} = \begin{bmatrix}\gamma_N{}^2 & 0\\ 0 & \gamma_N{}^{-2}\end{bmatrix}. \quad [5]$$

Thus, loss of ellipticity occurs when $\mathcal{L}(\lambda_N) = 0$ at some critical nominal stretch $\lambda_{N,C}$, where

$$\mathcal{L}(\lambda_N) = tr(\mathbf{B} - 2 - \gamma_{S,C}{}^2 = \lambda_N{}^2 + \frac{1}{\lambda_N{}^2} - 2 - \gamma_{S,C}{}^2. \quad [6]$$

Finite Element Simulations. We continue previously developed methods for replicating the uniaxial lateral compression of lipid monolayers using numerical modeling (39), integrating principles of nonlinear, large deformation solid mechanics with FE analysis. FE simulations are performed using the commercial software package Abaqus/Explicit 2021 (Dassault Systémes Americas Corp., Waltham, MA). The constitutive model is implemented into Abaqus/Explicit by writing the user subroutine VUMAT. We use two thin sheet models: a homogeneous model composed of a single material and a heterogeneous model composed of domains and a surrounding matrix of two respective materials. These models are built with the following unit system: length of micrometer in reference to the scale of FM micrographs utilized in the heterogeneous model (37), modulus unit of MPa in reference to experimental surface pressure measurements (37, 41, 81), and a unit mass of 10^{-9} g, in reference to the 1 g cm^{-3} density of water, for a dynamic explicit solver. For all matrix materials, the compressibility is dictated by the bulk modulus $K = 200$ MPa. This value is determined by the relation $K = 4C_1(1+\nu)/3(1-2\nu)$, where Poisson's ratio, $\nu \sim 0.495$ for a quasi-incompressible material.

Homogeneous model. A $10 \times 10 \times 1$ size thin square is meshed with 10,000 uniform two-dimensional plane strain shell elements (CPE4R, 4 node bilinear quadrilateral, reduced integration, with hourglass control).

Heterogeneous models. For the model shown in the main text figures, a FM image of a lipid monolayer before in-plane relaxation, of composition 7:3 DPPC:POPG with 10 wt% SP-B_{9-25}, at 25 °C and a surface pressure of 30mN m^{-1} as published previously (37), is imported into the Simpleware ScanIP software (Synopsys, Inc., Mountain View, CA) to segment out the domains from the matrix. For the models shown *SI Appendix*, Fig. S2, a FM image of an 8:2 DPPC:G_{M1} lipid monolayer at 30 °C and a surface pressure of 25mN m^{-1} and a FM image of a 5:5 DPPC:G_{M1} lipid monolayer at 30 °C and a surface pressure of 31mN m^{-1} as published previously (37), are segmented the same way. These segmentations are brought into ABAQUS and converted into sketches, which are then partitioned into $350 \times 350 \times 1$ size thin squares. The domains and matrix are then meshed with 149482 (7:3 DPPC:POPG), 231370 (8:2 DPPC:G_{M1}), and 244763 (5:5 DPPC:G_{M1}) total two-dimensional plane strain shell elements (97% CPE4R, 4 node bilinear quadrilateral, reduced integration, with hourglass control; 3% CPE3, 3 node linear triangle, reduced integration, with hourglass control). In addition, we provide approximately 60 units of excess matrix surrounding the domains to cushion the dynamic effects at the boundaries of the simulation, as seen in the initial morphology in Fig. 4. The matrix is given the material property described previously in *Materials and Methods*. The condensed domains are simulated by a neo-Hookean model with the same thickness and density, but approximately 100× stiffer than the matrix. This stiffness ratio is a parameter of the computational model that can be tuned to match the chosen system, depending on the degree of domain shape deformation that is observed experimentally. For this system, the following material equation is utilized, where $C_{10} = 100$ and $K = 4{,}000$. Note that $C_{10} = \mu/2$, where μ is shear modulus.

$$\psi_D = C_{10}(\bar{I}_1 - 3) + \frac{K}{2}(J-1)^2. \quad [7]$$

Boundary conditions. The use of plane strain in all models enforces a 2D geometric constraint. These models are then subjected to equal compression from both left and right boundaries to represent the loading condition in the experimental Langmuir trough setup. To minimize boundary effects in the heterogeneous models, velocity boundary conditions of 50 were applied for the left and right loads. Distribution of shear bands can be tuned via altering the compression, so to ensure well distributed shear bands between different scale of domains, the velocities were gradually ramped up from 0 to 50 before becoming constant when: $\lambda_N = 0.714$ (7:3 DPPC:POPG and 5:5 DPPC:G_{M1}) and $\lambda_N = 0.857$ (8:2 DPPC:G_{M1}). There are no boundary conditions on the top and bottom boundaries of the models' geometries. In all models, there is a general contact interaction property applied to all material with itself, to prevent unrealistic permeation of multiple elements. In the heterogeneous model, this same general contact interaction property is applied at the boundaries where the domains and matrix meet, preventing permeation of domains into the matrix, or vice versa.

Post processing. While simulations are run, data are recorded at regular intervals, providing frames for regular points along the compression of the model. Compression is measured by nominal stretch, $\lambda_N = L/L_0$, where L is the width of the deformed geometry in the loading direction. The initial distance between domains varies between experimental FM images. In order to most clearly represent domain reorganization, the simulation end points were chosen

where the morphologies share similar horizontal distances between domains to each other. For the model used in the main text, the FE results were taken at $\lambda_N \approx 0.7$ (Figs. 4 and 5). For the models used in *SI Appendix*, Fig. S2, the FE results were taken at $\lambda_N \approx 0.8$ (*SI Appendix*, Fig. S2, *Left*, DPPC:G_{M1} 8:2) and $\lambda_N \approx 0.4$ (*SI Appendix*, Fig. S2, *Right*, DPPC:G_{M1} 5:5). To measure the effective stress and relaxation of the FE models for the monolayer specimens, reaction force of the left boundary of each model is collected at each frame of the compression. This aggregate is calculated via a summation of the lateral component of the reaction force over all nodes of the left boundary. Due to the symmetric loading of the system, the right boundary could also be used, as it would exhibit approximately an equal and opposite reaction force response. To visualize shear strain localization in FE models and monitor shear band formation and behavior, the state-dependent variable defined in the VUMAT that tracks and updates the shear strain, γ_S (further explained in *SI Appendix*, section 1 and Eq. **S5**), is plotted on the deformed geometry of the models over the course of the compression. In Fig. 3, Case 3 and Fig. 4, comparative visualization is assisted by manually selecting minimum and maximum limits for shear strain values. The characteristics that define shear bands lie in the difference between the shear strain within the localized shear band vs. outside of the band. A strong shear band has a large difference in shear strain, while a weaker one has a small difference.

Data, Materials, and Software Availability. All study data are included in the article and/or supporting information.

ACKNOWLEDGMENTS. The work was supported in part by the NSF through grant CMMI-2433223 (to N.N.). K.Y.C.L. acknowledges support from The University of Chicago Materials Research Science and Engineering Center (MRSEC) (NSF/DMR–2011854) for this work. The work was partially supported by the NSF through MCB-1950525 (to K.Y.C.L.). A.D.G. acknowledges support from NIH National Institute of Biomedical Imaging and Bioengineering training grant T32EB009412 and a MRSEC-funded Kadanoff-Rice fellowship/Graduate Research Fellowship (DMR-2011854). A.R.C. gratefully acknowledges the partial support of PRIN-2022-PNRR MECHAVERSE. L.D. thanks the partial financial support to this research from: (a) the Italian Ministry of Universities and Research (MUR) in the framework of (a.1) the project DICAM-EXC, University of Trento, Departments of Excellence 2023-2027 (grant DM 230/2022); (a.2) the 2023-2025 PNRR CN ICSC Spoke 7 CUP E63C22000970007 grant, awarded to the University of Trento, Italy; (a.3) the grant PRIN-2022XLBLRX; and (b) the European Research Council through (b.1) the ERC-ADG-2021-101052956-BEYOND grant, and (b.2) the ERC-CoG 2022, SFOAM, 101086644 grant. M.F. gratefully acknowledges the partial support from MUR through the grant PRIN-2022ATZCJN. A.R.C., L.D., and M.F. also acknowledge the partial support from INDAM, Italian Institute of Theoretical and Applied Mathematics through the National Group of Mathematical Physics/Applied Mathematics. We would like to thank Shelli L. Frey for her previously published experimental data utilized in *SI Appendix* and the Illinois Mathematics and Science Academy for providing D.S. with research time and transportation.

Author affiliations: [a]Program in Biophysical Sciences, The University of Chicago, Chicago, IL 60637; [b]Department of Surgery, The University of Chicago, Chicago, IL, 60637; [c]Department of Structures for Engineering and Architecture, University of Napoli Federico II, Naples 80134, Italy; [d]Department of Civil, Environmental and Mechanical Engineering, University of Trento, Trento 38123, Italy; [e]Laboratoire de Physique de l'Ecole Normale Supérieure, Paris 75231, France; and [f]Department of Chemistry, James Franck Institute, and Institute for Biophysical Dynamics, The University of Chicago, Chicago, IL 60637

1. M. M. Van Schooneveld *et al*., Improved biocompatibility and pharmacokinetics of silica nanoparticles by means of a lipid coating: A multimodality investigation. *Nano Lett.* **8**, 2517–2525 (2008).
2. M. M. De Villiers, D. P. Otto, S. J. Strydom, Y. M. Lvov, Introduction to nanocoatings produced by layer-by-layer (LbL) self-assembly. *Adv. Drug Deliv. Rev.* **63**, 701–715 (2011).
3. A. Luchini, G. Vitiello, Understanding the nano-bio interfaces: Lipid-coatings for inorganic nanoparticles as promising strategy for biomedical applications. *Front. Chem.* **7**, 343 (2019).
4. K. Glasmästar, C. Larsson, F. Höök, B. Kasemo, Protein adsorption on supported phospholipid bilayers. *J. Colloid Interface Sci.* **246**, 40–47 (2002).
5. H. D. M. Follmann *et al*., Antiadhesive and antibacterial multilayer films via layer-by-layer assembly of TMC/heparin complexes. *Biomacromolecules* **13**, 3711–3722 (2012).
6. F. Persson *et al*., Lipid-based passivation in nanofluidics. *Nano Lett.* **12**, 2260–2265 (2012).
7. G. J. Ma *et al*., Lipid coating technology: A potential solution to address the problem of sticky containers and vanishing drugs. *VIEW* **3**, 20200078 (2022).
8. C. P. Collier, T. Vossmeyer, J. R. Heath, Nanocrystal superlattices. *Annu. Rev. Phys. Chem.* **49**, 371–404 (1998).
9. D. G. Schultz *et al*., Structure, wrinkling, and reversibility of Langmuir monolayers of gold nanoparticles. *J. Phys. Chem. B* **110**, 24522–24529 (2006).
10. K. E. Mueggenburg, X. M. Lin, R. H. Goldsmith, H. M. Jaeger, Elastic membranes of close-packed nanoparticle arrays. *Nat. Mater.* **6**, 656–660 (2007).
11. J. S. Silva, A. De Barros, C. J. L. Constantino, F. R. Simoes, M. Ferreira, Layer-by-layer films based on carbon nanotubes and polyaniline for detecting 2-chlorophenol. *J. Nanosci. Nanotechnol.* **14**, 6586–6592 (2014).
12. J. Goerke, Lung surfactant. *Biochim. Biophys. Acta (BBA) Rev. Biomembr.* **344**, 241–261 (1974).
13. A. Grace, P. Kwok, M. Kawke, Surfactant in middle ear effusions. *Otolaryngol. Neck Surg.* **96**, 336–340 (1987).
14. B. J. Glasgow *et al*., Tear lipocalins: Potential lipid scavengers for the corneal surface. *Invest. Ophthalmol. Vis. Sci.* **40**, 3100–3107 (1999).
15. R. Wüstneck *et al*., Interfacial properties of pulmonary surfactant layers. *Adv. Colloid Interface Sci.* **117**, 33–58 (2005).
16. S. A. Safran, *Statistical Thermodynamics of Surfaces, Interfaces, and Membranes* (CRC Press, ed. 1, 2018).
17. C. M. Knobler, R. C. Desai, Phase transitions in monolayers. *Annu. Rev. Phys. Chem.* **43**, 207–236 (1992).
18. H. Möhwald, Surfactant layers at water surfaces. *Rep. Prog. Phys.* **56**, 653–685 (1993).
19. C. M. Knobler, D. K. Schwartz, Langmuir and self-assembled monolayers. *Curr. Opin. Colloid Interface Sci.* **4**, 46–51 (1999).
20. A. Chachaj-Brekiesz, A. Wnętrzak, E. Lipiec, P. Dynarowicz-Latka, Surface interactions determined by stereostructure on the example of 7-hydroxycholesterol epimers - The Langmuir monolayer study. *Biochim. Biophys. Acta (BBA) Biomembr.* **1861**, 1275–1283 (2019).
21. O. Albrecht, H. Gruler, E. Sackmann, Polymorphism of phospholipid monolayers. *J. Phys.* **39**, 301–313 (1978).
22. D. Andelman, F. Brochard, C. Knobler, F. Rondelez, "Structures and phase transitions in Langmuir monolayers" in *Micelles, Membranes, Microemulsions, and Monolayers*, W. M. Gelbart, A. Ben-Shaul, D. Roux, Eds. (Springer New York, New York, NY, 1994), pp. 559–602.
23. V. M. Kaganer, H. Möhwald, P. Dutta, Structure and phase transitions in Langmuir monolayers. *Rev. Mod. Phys.* **71**, 779–819 (1999).
24. I. I. Perepichka, K. Borozenko, A. Badia, C. G. Bazuin, Pressure-induced order transition in nanodot-forming Diblock copolymers at the air/water interface. *J. Am. Chem. Soc.* **133**, 19702–19705 (2011).
25. D. H. Kim, S. Y. Kim, Effective morphology control of block copolymers and spreading area-dependent phase diagram at the air/water interface. *J. Phys. Chem. Lett.* **8**, 1865–1871 (2017).
26. D. H. Kim, S. Y. Kim, Universal interfacial control through polymeric nanomosaic coating for block copolymer nanopatterning. *ACS Nano* **14**, 7140–7151 (2020).
27. C. Helm, H. Möhwald, K. Kjaer, J. Als-Nielsen, Phospholipid monolayers between fluid and solid states. *Biophys. J.* **52**, 381–390 (1987).
28. A. Gopal, K. Y. C. Lee, Headgroup percolation and collapse of condensed Langmuir monolayers. *J. Phys. Chem. B* **110**, 22079–22087 (2006).
29. G. Espinosa, I. López-Montero, F. Monroy, D. Langevin, Shear rheology of lipid monolayers and insights on membrane fluidity. *Proc. Natl. Acad. Sci. U.S.A.* **108**, 6008–6013 (2011).
30. M. Buchanan, A matter of responding to stress. *Nat. Phys.* **13**, 620–620 (2017).
31. M. M. Lipp, K. Y. C. Lee, D. Y. Takamoto, J. A. Zasadzinski, A. J. Waring, Coexistence of buckled and flat monolayers. *Phys. Rev. Lett.* **81**, 1650–1653 (1998).
32. A. Gopal, K. Y. C. Lee, Morphology and collapse transitions in binary phospholipid monolayers. *J. Phys. Chem. B* **105**, 10348–10354 (2001).
33. C. Ybert, W. Lu, G. Möller, C. M. Knobler, Collapse of a monolayer by three mechanisms. *J. Phys. Chem. B* **106**, 2004–2008 (2002).
34. C. Ybert, W. Lu, G. Möller, C. M. Knobler, Kinetics of phase transitions in monolayers: Collapse. *J. Phys. Condens. Matter* **14**, 4753–4762 (2002).
35. B. Lin *et al*., Langmuir monolayers of gold nanoparticles. *Thin Solid Films* **515**, 5669–5673 (2007).
36. K. Y. C. Lee, Collapse mechanisms of Langmuir monolayers. *Annu. Rev. Phys. Chem.* **59**, 771–791 (2008).
37. L. Pocivavsek *et al*., Lateral stress relaxation and collapse in lipid monolayers. *Soft Matter* **4**, 2019 (2008).
38. L. Pocivavsek *et al*., Stress and fold localization in thin elastic membranes. *Science* **320**, 912–916 (2008).
39. S. Baoukina, L. Monticelli, H. J. Risselada, S. J. Marrink, D. P. Tieleman, The molecular mechanism of lipid monolayer collapse. *Proc. Natl. Acad. Sci. U.S.A.* **105**, 10803–10808 (2008).
40. S. L. Frey *et al*., Functional importance of the NH_2 -terminal insertion sequence of lung surfactant protein B. *Am. J. Physiol. Cell. Mol. Physiol.* **298**, L335–L347 (2010).
41. A. R. Carotenuto *et al*., Multiscale geometry and mechanics of lipid monolayer collapse in Current Topics in Membranes. *Elsevier* **87**, 1–45 (2021).
42. S. Kim *et al*., Surface pressure-area mechanics of water-spread poly(ethylene glycol)-based block copolymer micelle monolayers at the air-water interface: Effect of hydrophobic block chemistry. *Langmuir* **39**, 13546–13559 (2023).
43. J. Liu, Z. Y. Yin, L. Wu, P. Y. Hicher, Finite element implementation and application of a sand model in micropolar theory. *SN Appl. Sci.* **3**, 725 (2021).
44. C. Ege, M. K. Ratajczak, J. Majewski, K. Kjaer, K. Y. C. Lee, Evidence for lipid/cholesterol ordering in model lipid membranes. *Biophys. J.* **91**, L01–L03 (2006).

45. K. Kim, S. Q. Choi, Z. A. Zell, T. M. Squires, J. A. Zasadzinski, Effect of cholesterol nanodomains on monolayer morphology and dynamics. *Proc. Natl. Acad. Sci. U.S.A.* **110**, E3054–E3060 (2013).
46. M. M. Lipp, K. Y. Lee, A. Waring, J. A. Zasadzinski, Fluorescence, polarized fluorescence, and brewster angle microscopy of palmitic acid and lung surfactant protein B monolayers. *Biophys. J.* **72**, 2783–2804 (1997).
47. H. Mohwald, Phospholipid and phospholipid-protein monolayers at the air/water interface. *Annu. Rev. Phys. Chem.* **41**, 441–476 (1990).
48. H. M. McConnell, Structures and transitions in lipid monolayers at the air-water interface. *Annu. Rev. Phys. Chem.* **42**, 171–195 (1991).
49. M. M. Lipp, K. Y. C. Lee, J. A. Zasadzinski, A. J. Waring, Phase and morphology changes in lipid monolayers induced by SP-B protein and its amino-terminal peptide. *Science* **273**, 1196–1199 (1996).
50. F. Bringezu, J. Ding, G. Brezesinski, J. A. Zasadzinski, Changes in model lung surfactant monolayers induced by palmitic acid. *Langmuir* **17**, 4641–4648 (2001).
51. C. Valtierrez-Gaytan *et al*., Spontaneous evolution of equilibrium morphology in phospholipid-cholesterol monolayers. *Sci. Adv.* **8**, eabl9152 (2022).
52. H. E. Ries, Stable ridges in a collapsing monolayer. *Nature* **281**, 287–289 (1979).
53. H. Diamant, T. A. Witten, A. Gopal, K. Y. C. Lee, Unstable topography of biphasic surfactant monolayers. *Europhys. Lett. (EPL)* **52**, 171–177 (2000).
54. H. Diamant, T. A. Witten, C. Ege, A. Gopal, K. Y. C. Lee, Topography and instability of monolayers near domain boundaries. *Phys. Rev. E* **63**, 061602 (2001).
55. W. Lu, C. M. Knobler, R. F. Bruinsma, M. Twardos, M. Dennin, Folding Langmuir monolayers. *Phys. Rev. Lett.* **89**, 146107 (2002).
56. L. Pocivavsek *et al*., Geometric tools for complex interfaces: From lung surfactant to the mussel byssus. *Soft Matter* **5**, 1963 (2009).
57. K. Matan, R. B. Williams, T. A. Witten, S. R. Nagel, Crumpling a thin sheet. *Phys. Rev. Lett.* **88**, 076101 (2002).
58. S. Deboeuf, E. Katzav, A. Boudaoud, D. Bonn, M. Adda-Bedia, Comparative study of crumpling and folding of thin sheets. *Phys. Rev. Lett.* **110**, 104301 (2013).
59. P. Cicuta, D. Vella, Granular character of particle rafts. *Phys. Rev. Lett.* **102**, 138302 (2009).
60. D. Bigoni, *Nonlinear Solid Mechanics: Bifurcation Theory and Material Instability* (Cambridge Univ. Press, New York, NY, ed. 1, 2014).
61. N. Holten-Andersen *et al*., KL4 peptide induces reversible collapse structures on multiple length scales in model lung surfactant. *Biophys. J.* **101**, 2957–2965 (2011).
62. S. Garg, A. A. Thomas, M. A. Borden, The effect of lipid monolayer in-plane rigidity on in vivo microbubble circulation persistence. *Biomaterials* **34**, 6862–6870 (2013).
63. A. J. Kox, J. P. J. Michels, F. W. Wiegel, Simulation of a lipid monolayer using molecular dynamics. *Nature* **287**, 317–319 (1980).
64. C. Tempra, O. H. S. Ollila, M. Javanainen, Accurate simulations of lipid monolayers require a water model with correct surface tension. *J. Chem. Theory Comput.* **18**, 1862–1869 (2022).
65. B. D. Leahy *et al*., Geometric stability and elastic response of a supported nanoparticle film. *Phys. Rev. Lett.* **105**, 058301 (2010).
66. D. Steigmann, Ed., *The Role of Mechanics in the Study of Lipid Bilayers, CISM International Centre for Mechanical Sciences, Courses and Lectures* (Springer, Cham, 2017), vol. 577.
67. P. D. Olmsted, Perspectives on shear banding in complex fluids. *Rheol. Acta* **47**, 283–300 (2008).
68. S. Majumdar, R. Krishnaswamy, A. K. Sood, Shear banding in a yield stress bearing Langmuir monolayer. *Soft Matter* **7**, 7805 (2011).
69. A. Tordesillas, Q. Lin, J. Zhang, R. Behringer, J. Shi, Structural stability and jamming of self-organized cluster conformations in dense granular materials. *J. Mech. Phys. Solids* **59**, 265–296 (2011).
70. A. Carotenuto *et al*., Towards predicting shear-banding instabilities in lipid monolayers. *J. Mech. Behav. Biomed. Mater.* **141**, 105743 (2023).
71. W. Seki, S. N. Atluri, Analysis of strain localization in strain-softening hyperelastic materials, using assumed stress hybrid elements. *Comput. Mech.* **14**, 549–585 (1994).
72. P. Rosakis, Ellipticity and deformations with discontinuous gradients in finite elastostatics. *Arch. Ration. Mech. Anal.* **109**, 1–37 (1990).
73. R. Abeyaratne, J. K. Knowles, Equilibrium shocks in plane deformations of incompressible elastic materials. *J. Elast.* **22**, 63–80 (1989).
74. I. C. Shieh, J. A. Zasadzinski, Visualizing monolayers with a water-soluble fluorophore to quantify adsorption, desorption, and the double layer. *Proc. Natl. Acad. Sci. U.S.A.* **112**, E826–E835 (2015).
75. C. O. Ciutara, S. V. Iasella, B. Huang, S. Barman, J. A. Zasadzinski, Evolution of interfacial mechanics of lung surfactant mimics progression of acute respiratory distress syndrome. *Proc. Natl. Acad. Sci. U.S.A.* **120**, e2309900120 (2023).
76. G. Del Piero, D. R. Owen, Structured deformations of continua. *Arch. Ration. Mech. Anal.* **124**, 99–155 (1993).
77. L. Deseri, D. R. Owen, Moving interfaces that separate loose and compact phases of elastic aggregates: A mechanism for drastic reduction or increase in macroscopic deformation. *Continuum Mech. Thermodyn.* **25**, 311–341 (2013).
78. L. Deseri, D. R. Owen, Stable disarrangement phases of elastic aggregates: A setting for the emergence of no-tension materials with non-linear response in compression. *Meccanica* **49**, 2907–2932 (2014).
79. L. Deseri, D. R. Owen, Elasticity with hierarchical disarrangements: A field theory that admits slips and separations at multiple submacroscopic levels. *J. Elast.* **135**, 149–182 (2019).
80. B. G. Moore, C. M. Knobler, S. Akamatsu, F. Rondelez, Phase diagram of Langmuir monolayers of pentadecanoic acid: Quantitative comparison of surface pressure and fluorescence microscopy results. *J. Phys. Chem.* **94**, 4588–4595 (1990).
81. Z. Al-Rekabi, S. Contera, Multifrequency AFM reveals lipid membrane mechanical properties and the effect of cholesterol in modulating viscoelasticity. *Proc. Natl. Acad. Sci. U.S.A.* **115**, 2658–2663 (2018).